ACS OMEGA

Open Access

This article is licensed under CC-BY-NC-ND 4.0

http://pubs.acs.org/journal/acsodf

Article

Smart Magnetic Nanocarriers for Codelivery of Nitric Oxide and Doxorubicin for Enhanced Apoptosis in Cancer Cells

Bijaideep Dutta, Sandeep B. Shelar, Ananya Nirmalraj, Sonali Gupta, Kanhu C. Barick,* Jagriti Gupta, and Puthussericka A. Hassan*

Cite This: *ACS Omega* 2023, 8, 44545−44557

Read Online

ACCESS | Metrics & More | Article Recommendations | Supporting Information

ABSTRACT: Extremely short half-life therapeutic molecule nitric oxide (NO) plays significant roles in the functioning of various physiological and pathological processes in the human body, whereas doxorubicin hydrochloride (DOX) is a clinically important anticancer drug widely used in cancer chemotherapy. Thus, the intracellular delivery of these therapeutic molecules is tremendously important to achieve their full potential. Herein, we report a novel approach for the development of highly water-dispersible magnetic nanocarriers for codelivery of NO and DOX. Primarily, bifunctional magnetic nanoparticles enriched with carboxyl and thiol groups were prepared by introducing cysteine onto the surface of citrate-functionalized Fe_3O_4 nanoparticles. DOX was electrostatically conjugated onto the surface of bifunctional nanoparticles via carboxyl moieties, whereas the thiol group was further nitrosated to provide NO-releasing molecules. The developed magnetic nanocarrier exhibited good aqueous colloidal stability, protein resistance behavior, and high encapsulation efficacy for NO (65.5%) and DOX (85%), as well as sustained release characteristics. Moreover, they showed superior cytotoxicity toward cancer (A549 and MCF-7) cells via apoptosis induction over normal (WI26VA4) cells. Specifically, we have developed magnetic nanocarriers having the capability of dual delivery of NO and DOX, which holds great potential for combinatorial cancer treatment.

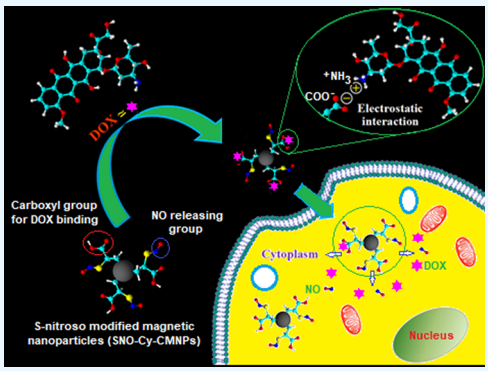

1. INTRODUCTION

Despite significant advances in medical science and technology, cancer remains the gravest threat for human beings, and it has been one of the protruding reasons of death across the globe for the past few decades.[1] It refers to the anomalous behavior and uncontrolled growth of cells without relying on the signals that control the cell behavior and eventually spreading to other regions of the body. Chemotherapy, radiotherapy, and surgery are the most common strategies for cancer management. Among these, chemotherapy has been prevalent over the years due to its simplicity and accessibility in treating cancer patients.[2−4] The main challenges in conventional chemotherapy are the side effects allied with nonspecific delivery of the active ingredients followed by their toxicity to normal cells, heavy dosage, severe multidrug resistance, and so forth.[5−7] To alleviate all these shortcomings, nanocarriers with the ability to codeliver chemotherapeutic drugs and other therapeutic molecules to the site of action are the emerging choice by the researchers, which can exhibit augmented cancer cell-killing efficacy.[8−12]

After the discovery of nitric oxide (NO), a water-soluble short-lived free radical gas in 1980, as a signaling probe in cardiovascular arrangement, it has attained tremendous interest in various biological functions starting from angiogenesis, apoptosis, neurotransmission, and immune response.[13,14] It is getting synthesized by homodimeric heme-containing nitric oxide synthase (NOS) enzymes and produced in mammalian cells in appropriate proportion to maintain the key signaling routes for various physiological processes.[15] The central dogma in NO signaling is that NO, being a tiny neutral lipophilic gas, readily transduces via diffusion over cell membranes from one cell to another to reach its main target, soluble gyanylylcyclase (sGC). NO then binds to the heme iron of sGC to activate and generate cyclic guanosine monophosphate (cGMP).[16] This in turn activates the downstream kinases (cGMP-regulated protein kinases) and ion channels to regulate a variety of physiological processes like cardiovascular function, RBC and platelet activity, metabolic regulation, neurotransmission, host defense, and cancer.[17−22]

Recent studies on NO have shown great promise in anti-inflammatory as well as anticancer properties, which are essentially concentration dependent.[23] At a very low concentration (pM-nM), it helps in vasodilation to augment

Received: May 27, 2023
Revised: October 30, 2023
Accepted: October 31, 2023
Published: November 15, 2023

© 2023 The Authors. Published by American Chemical Society

cancer cell infiltration, whereas at an elevated concentration (μM-mM), it turns out to be a killer one by oxidation and nitrosative stress.[24,25] Therefore, the presence of the required amount of NO in the tumor microenvironment (TME) inhibits the expression of mammalian HIF-1α, base-excision DNA repair enzyme, and NF-kB activation and the overexpression of a transmembrane P-glycoprotein (P-gp) which is involved in ATP-dependent drug effluxing from cancer cells.[26,27] Moreover, NO is also very much reactive with superoxide ($O_2^{\cdot -}$) to generate more highly reactive $ONOO^-$ to induce the oxidation of DNA and proteins and further sensitizing radiotherapy, phototherapy, and chemodynamic therapy.[28,29] Due to the significant role of NO in inhibiting the tumor growth and subsequent progression, there is ever increasing curiosity in maneuvering the therapeutic potential of NO to overcome the multidrug resistance (MDR) for cancer cell killing. As NO is a free radical with very limited stability, a prolific design of NO-releasing donor moieties with proper release characteristics at the desired concentration range is a challenging task.

Among several low-molecular-weight NO donor molecules, S-nitrosothiols, namely, S-nitrosoglutathione (GSNO) and S-nitrosocysteine, have been found in biological systems that can spontaneously give rise to NO by hemolytic cleavage of the S−N bond at elevated glutathione concentrations in the tumor tissue. However, due to their limitation in delivering therapeutic dosage of NO at the target site, NO donors or NO prodrugs are allied or attached with smart nanomaterials which can increase the stability of the NO donor in comparison to the free NO donor molecule, augment the NO loading efficiency, improve the NO concentration at the site of action by virtue of enhanced permeability and retention (EPR) effect, and thereby trigger the on-demand NO release using different stimuli for a prolonged period of time.[30] To further improve the outcome of NO-releasing nanomaterials, chemotherapeutic drugs have been combined on the same platform. The down regulation of P-gp by NO molecules essentially enhances the drug uptake by reversing the MDR. Thus, several NO-releasing nanomaterials (liposomes, polymeric/inorganic nanoparticles) have been scrutinized in combination with chemotherapeutic drugs for the controlled NO delivery and synergistic cancer cell killing.[31−38] Among others, Fe_3O_4 magnetic nanoparticles (MNPs) are also extremely important nanocarriers for delivery of NO due to their nontoxic nature (biocompatible) and unique physicochemical and magnetic properties. For example, Yuan et al. prepared NO donor-loaded Fe_3O_4-polydopamine core−shell nanoparticles for biofilm treatment.[35] Santos et al. have also prepared PEGylated magnetic nanocarriers for NO delivery.[38] Although various MNPs have been designed with the objective of achieving enhanced therapeutic efficacy, spatiotemporal control for the delivery of the required dosage of NO is yet to be accomplished. Herein, L-cysteine conjugated magnetic nanocarriers (SNO-Cy-CMNPs) were developed with a soft-chemical approach for the codelivery of DOX and NO in a sustained manner, which have the capacity to enhance the cellular apoptosis in lung cancer (A549) and breast cancer (MCF-7) cell lines. Further, being magnetic in nature, these nanocarriers can be targeted to the site of interest using an external magnetic field in addition to their passive targeting ability.

2. MATERIALS AND METHODS

2.1. Materials. Iron(II) chloride tetrahydrate, iron(III) chloride hexahydrate, *N*-hydroxysuccinimide (NHS), bovine serum albumin (BSA), and Griess reagent were obtained from Sigma-Aldrich, Germany. Ammonia (25%), citric acid monohydrate, dimethyl sulfoxide (DMSO), and 1-ethyl-3-(3-(dimethylamino)propyl) carbodiimide (EDC) were purchased from SDFCL, Mumbai, India. L-cysteine hydrochloride monohydrate and sodium nitrite were purchased from SRL, Mumbai, India. Dulbecco's modified eagle medium (DMEM), fetal calf serum (FCS), antibiotics, MTT reagent (Thiazolyl blue tetrazolium bromide), and dialysis membrane-60 were procured from Himedia Laboratories Pvt. Ltd., Mumbai, India. DOX was received as a kind gift from Advanced Centre for Treatment, Research and Education in Cancer (ACTREC), Navi Mumbai, India. A549 (human lung cancer), MCF-7 (breast cancer) and WI26VA4 (human lung normal) cells were received as kind gifts from Radiation Biology & Health Science Division, BARC, Mumbai.

All aqueous solutions were prepared using deionized water from a Millipore-Milli Q system (resistivity ∼18 MΩ cm). The acetate buffer (AB, pH 5.5) and phosphate-buffered saline (PBS, pH 7.4) were prepared by using standard protocols. *All chemicals* used were of *AR grade unless* otherwise specified and used as such without further treatment.

2.2. Synthesis of Citrate and Cysteine-Functionalized Magnetic Nanoparticles. Citric acid-functionalized magnetic nanoparticles (CMNPs) were synthesized by coprecipitation of ferrous and ferric ions (1:2 molar ratio) in the presence of ammonia as reported elsewhere.[39] Briefly, $FeCl_2.4H_2O$ (1.988 g) and $FeCl_3.6H_2O$(5.406 g) were dissolved in 80 mL of water in a round-bottom flask. The reaction temperature was slowly increased to 70 °C under a N_2 atmosphere with constant stirring and maintained for 30 min at 70 °C. Then, 20 mL of ammonia solution was added instantaneously to it and kept at the same temperature for another 30 min. After this, 4ml of aqueous solution of citric acid (0.5 g/mL) was added, and the reaction temperature was slowly raised up to 90 °C under reflux and reacted for 60 min with continuous stirring. The resulting black-colored precipitate (CMNPs) was thoroughly washed with deionized water by magnetic separation.

In order to introduce bifunctionality (thiol and carboxyl groups), L-cysteine (amino acid) was conjugated onto the surface of CMNPs by an EDC-NHS coupling reaction. In a typical synthesis, 800 mg of CMNPs (dried at room temperature) was added to a round-bottom flask containing 10 mL of DMSO and 12 mL of H_2O and sonicated for 15 min. An aqueous solution of EDC (3.44 mmol, 441.6 mg dissolved in 5 mL of H_2O) was then added to the flask and sonicated for another 15 min. Then, an aqueous solution of NHS (2.3 mmol, 397.8 mg dissolved in 5 mL H_2O) was added to the reaction flask and sonicated for another 15 min (the ratio of NHS/EDS = 1.5). Using a mechanical stirrer, the reaction was further stirred at 400−500 rpm for a period of 60 min. The dispersion was then decanted by magnetic separation, and the activated nanoparticles were then washed twice with deionized water to remove any remnants of EDC and NHS and reaction byproducts. The activated particles (725 mg, yield = 90.6%) were then resuspended in 20 mL of deionized water, and 303.6 mg of L-cysteine was added to it. Stirring was continued at 400−500 rpm over a period of 12 h. The formed cysteine-

https://doi.org/10.1021/acsomega.3c03734
ACS Omega 2023, 8, 44545−44557

functionalized magnetic nanoparticles (Cy-CMNPs) were collected by magnetic separation. Both CMNPs and Cy-CMNPs were dried at room temperature for solid-phase characterization, while solution-phase studies were performed with respective aqueous suspensions.

2.3. Introduction of NO Groups onto the Surface of Cy-CMNPs. Cy-CMNPs were subjected to further treatment for nitrosation of the S−H group of cysteine. In a typical reaction, 200 mg of the dried Cy-CMNPs were dispersed in 64 mL of H_2O and sonicated for 5 min, and then, 60 mM sodium nitrite solution (165.6 mg of $NaNO_2$ in 40 mL of H_2O) was added to it. The reaction mixture was stirred using a mechanical stirrer at 400−500 rpm for a period of 1 h. The formed nitrosated cysteine-functionalized magnetic nanoparticles (SNO-Cy-CMNPs) were obtained by magnetic separation and then washed twice using deionized water. Part of the SNO-Cy-CMNPs was dried for solid-phase characterization, and the remaining was kept in suspension for solution-phase studies. The supernatant solution obtained after magnetic separation of SNO-Cy-CMNPs as well as their washing solution were used for determining the percentage of NO loaded onto the surface of the nanocarrier (by conversion of -SH to -SNO via nitrosation) by the Griess reagent assay using a UV−visible spectrophotometer. The assay was based on the reaction between nitrite, sulfanilamide, and N-1-naphthylethylenediamine dihydrochloride, which can produce a compound with maximum absorption at 540 nm.[22,40] For this, 50 μL of supernatant/washing solution was mixed with 100 μL of Griess reagent, and the mixture was incubated for 15 min under stirring at 37 °C in the dark. Then, the absorbance was measured using a microplate reader at 540 nm, and NO uptake was quantified against the standard plot prepared under a similar condition using sodium nitrite (concentration range = 0−100 μM, R^2 = 0.9991).

2.4. Characterization of the Synthesized CMNPs, Cy-CMNPs, and SNO-Cy-CMNPs,. The physicochemical characterization of CMNPs, Cy-CMNPs, and SNO-Cy-CMNPs was performed by Fourier transform infrared spectroscopy (FTIR, Bomem MB series), X-ray diffraction (XRD, Rigaku diffractometer), and transmission electron microscopic (TEM, Philips CM 200). Thermogravimetric analysis (TGA) of samples was carried out at a scan rate of 10 °C/min under a N_2 atmosphere using a Mettler Toledo TG/DSC stare system. The average hydrodynamic diameter and light scattering intensity were measured using a Malvern 4800 Autosizer employing a 7132-digital correlator. The pH-dependent zeta potentials were monitored using a Zetasizer, Nanoseries (Malvern). The colloidal stability of SNO-Cy-CMNPs (0.1 mg/mL) was investigated by monitoring the changes in the hydrodynamic diameter, light scattering intensity, and absorbance with time. The changes in the absorbance of aqueous suspension SNO-Cy-CMNPs were performed by a JASCO V-650, UV−visible spectrophotometer at a wavelength of 350 nm. The protein-particle interaction studies was performed by measuring the absorbance at 280 nm as well as the zeta potential upon interacting SNO-Cy-CMNPs (0.02 mg/mL) with BSA (0.025 mg/mL) in PBS solution for different time intervals. The field and temperature dependence magnetization studies were performed by a physical property measurement system, Quantum Design.

2.5. Drug Loading and Release Studies. In order to estimate the drug loading and release behavior of SNO-Cy-CMNPs, DOX was used as a model drug. DOX was electrostatically conjugated onto the surface of the nanocarrier by interacting different amounts of SNO-Cy-CMNPs (0, 60, 100, and 140 μg of Fe) with 10 μL of DOX (1 mg/mL) as reported elsewhere.[41] Then, the amount of DOX loading was calculated by measuring the fluorescence intensity of the supernatant (λ_{ex} = 485 and λ_{em} = 590 nm) obtained after separation of DOX-loaded SNO-Cy-CMNPs (DOX-SNO-Cy-CMNPs) using a SYNERGY/H1 microplate reader (BioTeK, Germany). The loading efficiency (w/w %) was determined using the following formula:[41]

$$\text{loading efficiency}(\%) = \frac{I_{DOX} - I_S - I_w}{I_{DOX}} \times 100$$

where I_{DOX} is the fluorescence intensity of pure DOX solution, I_S is the fluorescence intensity of the supernatant, and I_W is the fluorescence intensity of washed DOX (physically adsorbed DOX). The drug-loading content was obtained from the following formula:[41]

$$\text{drug loading content}(\%) = \frac{\text{weight of encapsulated DOX}}{\text{weight of nano carrier}} \times 100$$

The encapsulation efficiency was also reconfirmed by the absorbance intensity using a UV−visible spectrophotometer as reported earlier.[10,42] For the release study, drug-loading experiments were performed at an increased scale with a drug-to-particle (expressed in terms of Fe) ratio of 1:14 (w/w). The drug release studies were carried out in AB pH 5.5 and PBS pH 7.4 at 37 °C under reservoir-sink conditions. DOX-SNO-Cy-CMNPs (5 mg) were immersed into 3 mL of buffer medium (AB pH 5.5 or PBS 7.4) and then transferred into a dialysis bag. The dialysis was performed against 150 mL of respective release medium under constant stirring at 37 °C. The amount of DOX released was determined by measuring the fluorescence intensity at 590 nm (λ_{ex} = 485) using a microplate reader against the standard plot prepared (concentration range = 0.3−7.6 μg/mL, R^2 = 0.9995) under similar conditions. Each experiment was performed in triplicates, and standard deviation is given in the plots.

2.6. NO Uptake and Release Studies. The intracellular uptake of NO was quantified by the Griess reagent assay as discussed earlier. Briefly, A549 and MCF-7 cells were seeded in a 6-well plate for 24 h followed by the treatment with known amounts of SNO-Cy-CMNPs and DOX-SNO-Cy-CMNPs. After 4 and 24 h of incubation, the cells were washed with PBS (thrice). The cells were further lysed using 1% Triton-X 100 in distilled water. The cell lysate was then centrifuged at 10,000 rpm for 10 min. The supernatant was then taken out for the Griess reagent assay.

NO release studies were performed in a cellular mimicking environment under reservoir-sink conditions at 37 °C as well as in intracellular conditions using cancer cell lines (A549 and MCF-7) and quantified by the Griess reagent assay through a UV−visible spectrophotometer. For NO release under reservoir-sink conditions, a known amount of the SNO-Cy-CMNPs was incubated in AB pH 5.5/PBS pH 7.4). Then, it was transferred into a dialysis bag (MWCO = 14 kDa). The dialysis was performed against 50 mL of respective release medium under constant stirring at 37 °C. At a predetermined interval, 50 μL of the above solution from the external medium was taken out and mixed with 100 μL of the Griess reagent assay. For intracellular NO release (in the A549 and MCF-7

https://doi.org/10.1021/acsomega.3c03734
ACS Omega 2023, 8, 44545−44557

cell lines), the cells were first seeded in a 96-well plate for 24 h. Then, they were treated with a known amount of SNO-Cy-CMNPs/DOX-SNO-Cy-CMNPs for 24 h (at a total volume of 200 μL). After 24 h of incubation, the culture medium of each well was replaced by a fresh medium to investigate the release behavior of NO. For this, 50 μL of medium was taken from the wells at different intervals of time (0, 0.5, 1, 2, 4, and 24 h) and mixed with 100 μL of Griess reagent for quantification of NO release.

2.8. Cell Viability Studies by MTT Assay. The cytotoxicity studies were performed with A549, MCF-7, and WI26VA4 cells by the MTT assay. A549 is an epithelial cell that was isolated from the lung of a 58-year-old, white male with carcinoma (ATCC No. CRM-CCL-185). MCF-7 was derived from the pleural effusion of a 69-year-old female suffering from breast adenocarcinoma (ATCC No. HTB-22). WI26VA4 is an SV40 virus-transformed derivative of WI-26, a human diploid fibroblast cell line from the embryonic lung tissue (ATCC No. CCL-95.1). The cells (5000) were seeded overnight in 96-well plates containing 100 μL of DMEM supplemented with 10% FCS and antibiotics (100 U/ml penicillin and 100 mg/mL streptomycin) in a humidified atmosphere of 5% CO_2 at 37 °C. Then, different amounts of pure DOX and DOX-SNO-Cy-CMNPs (with DOX concentration of 0, 0.5, 1.0, 1.5, 2.0, 2.5, and 3.0 μM) were added to the cells, and these were incubated for another 48 h in culture conditions. Then, the culture medium of each well was replaced by a fresh medium having 0.5 mg/mL MTT and further incubated for 3 h. After this, the MTT solution was aspirated, and the formed formazan crystals were solubilized by adding 100 μL of DMSO to each well. For the calculation of cytotoxicity, the absorbance of each well was measured in a microplate reader at 544 nm. The cell viability was obtained by comparing the absorbance of the treated cells with that of control cells, which was considered as 100%. Each experiment was accomplished in triplicate, and the standard deviation was specified in the plot. The cytotoxicity study of DOX-Cy-CMNPs was also performed for comparative purposes at the same concentration. MTT assay was also performed on A549, MCF-7, and WI26VA4 cells after 48 h of incubation with CMNPs, Cy-CMNPs, and SNO-Cy-CMNPs up to 100 μg. The morphological changes of the cells upon the various treatments were also captured using a bright-field microscope.

2.9. Cellular Internalization by Confocal Microscopy and Flow Cytometry. Cellular internalization studies were performed with A549, MCF-7, and WI26VA4 cells using confocal microscopy and flow cytometry. For imaging, cells (0.5×10^6) were seeded on glass coverslips and cultured overnight. The cells were then treated with DOX and DOX-SNO-Cy-CMNPs (at a DOX concentration of 5 μM) for 3 h under culture conditions, followed by washing with PBS. The cells were mounted on a glass slide in cell mounting medium (Invitrogen, USA) containing DAPI for nuclear staining and then imaged by confocal microscopy (FV 3000, Olympus) using a red filter for DOX and a blue filter for DAPI. For flow cytometry analysis, the cells were cultured on 6-well plates at 37 °C. When the cells reached approximately 70−80% confluence, the medium containing DOX/DOX-Cy-CMNPs/DOX-SNO-Cy-CMNPs (at a DOX concentration of 5 μM) was subsequently added and incubated for 3 h. The cells were then harvested by trypsinization and resuspended in culture medium for flow cytometry analysis (FL-2 channel) using a flow cytometer (CyFlow Space, Sysmex Partec GmbH, Germany). Ten thousand gated events were collected and analyzed with the FlowJo software.

2.10. Cell Cycle and Apoptosis Detection by Flow Cytometry. For cell cycle analysis, both A549 and MCF-7 cells were treated with pure DOX and DOX-SNO-Cy-CMNPs (5 μM) for 24 h. Cells were then harvested by trypsinization and washed with PBS two to three times. Cells were centrifuged at 2500 rpm for 5 min, the supernatant was discarded, and then the cells were fixed by 70% ethanol with continuous vortexing until single cell suspension is formed. Cells were centrifuged again and resuspended in PBS to make a cell suspension of 1×10^6 cells/ml. Cells were then treated with RNase A at a concentration of 50 μg/mL for 30 min and then treated with propidium iodide at a concentration of 100 μg/mL for 10 min. The cell suspension was immediately subjected to flow cytometry analysis to record the status of the cell cycle (Cyflow Cube 6, Sysmex). Cell apoptosis was investigated using an annexin V-FITC (fluorescein isothiocyante)/PI (propidium iodide) apoptosis detection kit (Sigma-Aldrich, APOAF). For this study, cells were cultured in 60 mm culture dish overnight and then treated with free DOX, SNO-Cy-CMNPs, and DOX-SNO-Cy-CMNPs with a drug concentration of 5 μM for 24 h. Afterward, the cells were harvested and resuspended in annexin V binding buffer at a concentration of 1 million cells/ml. Cells were then treated with the annexin V antibody tagged with FITC and PI for 10 min at room temperature. Cells were immediately analyzed using flow cytometry (Sysmex, Cube 8), and dot blots of annexin V vs PI were recorded for around 20,000 cells.

2.11. Statistical Analysis. All results and measurements were shown as the mean ± SD (standard deviation). Comparisons between the mean values of different groups were analyzed by unpaired two-tailed Student's t test (using t test calculator, GraphPad), where (*) $p < 0.05$ was considered statistically significant and (**) $p < 0.01$ was considered highly statistically significant.

3. RESULTS AND DISCUSSION

3.1. Structural Analysis, Colloidal Stability Assay, and Magnetic Studies. A bifunctional nanocarrier (enriched with carboxyl and thiol groups) was precisely designed with the objective of the delivery of NO in association with a chemotherapeutic drug for enhanced apoptosis in cancer cells. This was achieved by the introduction of a biocompatible amino acid, cysteine, onto the surface of CMNPs via EDC-NHS coupling. The thiol groups of the bifunctional nanocarriers were converted to S-NO by nitrosation, and anticancer drug, DOX was electrostatically conjugated as shown in

Scheme 1. Schematic Representation of Cysteine Functionalization, Nitrosation, and DOX Loading

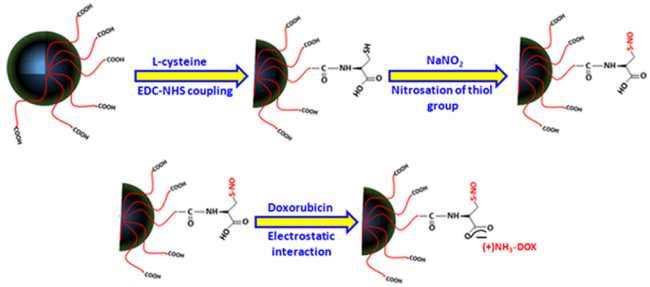

https://doi.org/10.1021/acsomega.3c03734
ACS Omega 2023, 8, 44545−44557

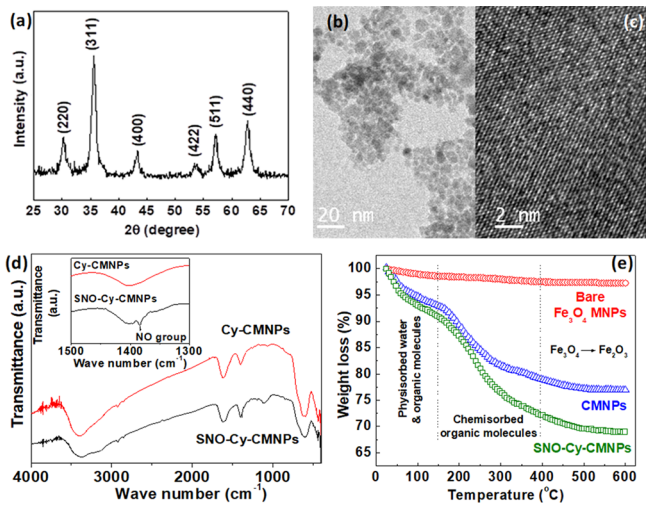

Figure 1. (a) XRD pattern of SNO-Cy-CMNPs showing different lattice planes of the inverse spinel magnetite (Fe_3O_4) phase. (b) TEM image and (c) high-resolution TEM micrographs of SNO-Cy-CMNPs revealing the formation of roughly spherical nanoparticles and (220) lattice plane, respectively. (d) FTIR spectra of Cy-CMNPs and SNO-Cy-CMNPs showing the presence of vibrational bands corresponding to respective functional moieties. (e) TGA plots of bare Fe_3O_4, CMNPs, and SNO-Cy-CMNPs revealing the enhancement of weight loss upon organic modification (bare Fe_3O_4 MNPs were prepared in a similar method without using any organic coating agent for comparative purpose).

Scheme 1 for the augmented benefit in therapeutic modules in cancer treatment.

The shape, size, and crystallographic phase of SNO-Cy-CMNPs were investigated by XRD and TEM analyses. The appearance of broad and intense diffraction peaks at around 30, 35, 43, 53, 57, and 62° (Figure 1a) corresponding to the highly crystalline (220), (311), (400), (422), (511), and (440) lattice planes suggested the formation of an inverse spinel magnetite (Fe_3O_4) phase.[43] The crystallite sizes were calculated to be around 10 nm from X-ray line broadening by using Scherrer's formula. This result was further validated using TEM micrograph (Figure 1b) which clearly shows the formation of roughly spherical nanoparticles of average size 10 nm. The average interplanar distance of SNO-Cy-CMNPs was measured to be ~0.30 nm (Figure 1c), which corresponds to the (220) plane of Fe_3O_4.[44] The organic modification on the surface of the nanocarriers was explored by FTIR and TGA. The vibration band at ~585 cm^{-1} in the FTIR spectra of Cy-CMNPs and SNO-Cy-CMNPs is associated with the stretching mode of Fe−O of Fe_3O_4.[10] The vibrational bands observed at 1612 and 1400 cm^{-1} correspond to the asymmetric and symmetric stretching of COO^-groups (citrate and cysteine), respectively.[39] The CH stretching vibrations of citrate and cysteine molecules present on the surface of MNPs appeared in the range of 2800−3000 cm^{-1}.[45] The broad band observed in the region of 3000−3500 cm^{-1} can be associated with the stretching vibration of carboxylic OH group of cysteine.[45] The successful conversion of Cy-CMNPs into SNO-Cy-CMNPs was evident from the appearance of the

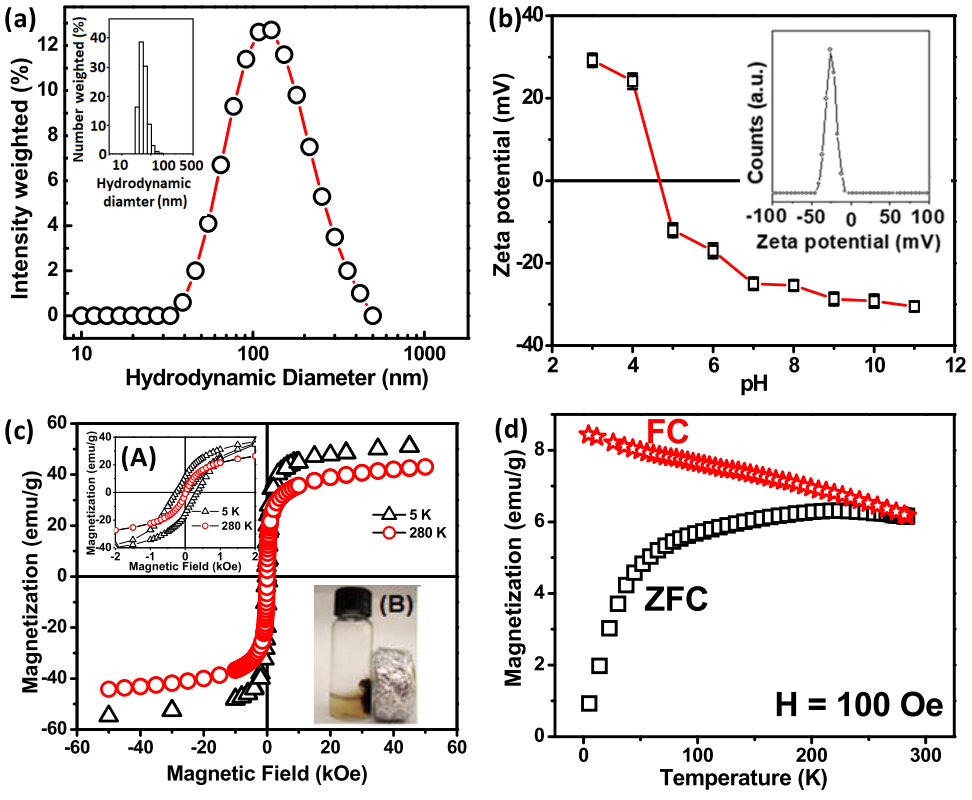

Figure 2. (a) Intensity-weighted particle size distribution plot of SNO-Cy-CMNPs obtained from DLS studies (inset shows the corresponding number-weighted particle size distribution), (b) their pH-dependent zeta potential plot indicating the variation of surface charge (inset show its zeta potential at physiological medium, PBS pH 7.4), (c) M vs H plots of SNO-Cy-CMNPs at 5 and 280 K (inset A: M. vs H plot at low field region; inset B: photograph showing attraction of particles toward external magnet of field strength 0.25 kOe), and (d) ZFC-FC plot of SNO-Cy-CMNPs at an applied field of 100 Oe.

https://doi.org/10.1021/acsomega.3c03734
ACS Omega 2023, 8, 44545−44557

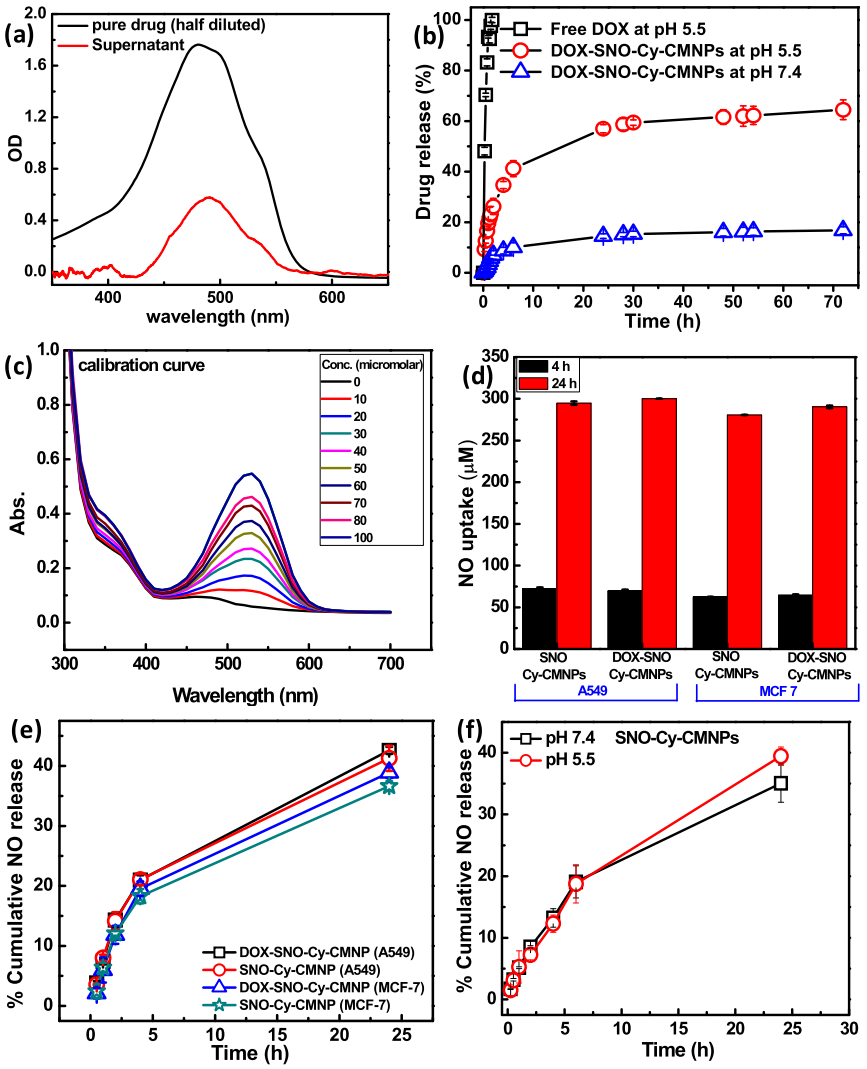

Figure 3. (a) Absorption spectra of DOX loading in SNO-Cy-CMNPs. (b) Drug release profile of free DOX and DOX-SNO-Cy-CMNPs at different pH at 37 °C under reservoir-sink condition. (c) Standard calibration curve prepared using Griess reagent for NO determination. (d) Intracellular uptake of SNO-Cy-CMNPs and DOX- SNO-Cy-CMNPs in A549 and MCF-7 cell lines at 4 and 24 h. (e) Intracellular (A549 and MCF-7) NO release profile of SNO-Cy-CMNPs and DOX- SNO-Cy-CMNPs. (f) NO release profile of SNO-Cy-CMNPs at two different pH (7.4 and 5.5).

vibrational mode corresponding to the N−O group at 1380 cm^{-1} in the FTIR spectrum of SNO-Cy-CMNPs.[46] TGA plots of CMNPs and SNO-Cy-CMNPs showed three steps of thermal decomposition with a total weight loss of about 23 and 31%, respectively. The first step weight loss can be attributed to the removal of physisorbed water and organic molecules, whereas the second step weight loss corresponds to the removal of chemisorbed organic molecules. The third step weight loss beyond 400 °C can be associated with the structural transition of Fe_3O_4 to Fe_2O_3.[39] However, the TGA plot of bare Fe_3O_4 MNPs exhibited weight loss of about 5% over the whole temperature range due to the loss of physisorbed water and hydroxyl groups from the surface of Fe_3O_4 particles and their structural transition. It is noteworthy to mention that the observed higher weight loss in the TGA analysis of SNO-Cy-CMNPs over CMNPs clearly suggests their successful organic modification.

Light scattering measurements were performed on the aqueous dispersion of SNO-Cy-CMNPs to explore the hydrodynamic diameter and surface charge of particles as well as their colloidal stability. The aqueous dispersion of SNO-Cy-CMNPs showed an intensity-weighted average hydrodynamic diameter of about 122 nm (Figure 2a). The corresponding number average hydrodynamic diameter was also determined using light scattering software and found to be around 35 nm (inset of Figure 2a). The observed higher number average diameter by DLS than TEM could be ascribed to the associated hydrated organic layer on the surface of the particles.[47,48] Moreover, the polydispersity in size (d) and particle aggregation will lead to higher average hydrodynamic diameter as DLS is weighted toward large sizes (d^6 dependence of the scattering intensity on particle size). Further, the colloidal stability of SNO-Cy-CMNPs was investigated by monitoring the changes in the hydrodynamic diameter, light scattering intensity, and absorbance with time (Figure S1a−c, Supporting Information). The nominal changes in the hydrodynamic diameter, light scattering intensity, and absorbance with time suggested the good aqueous dispersibility and colloidal stability of SNO-Cy-CMNPs. Further, the typical UV−visible absorption spectrum of SNO-Cy-CMNPs

https://doi.org/10.1021/acsomega.3c03734
ACS Omega 2023, 8, 44545−44557

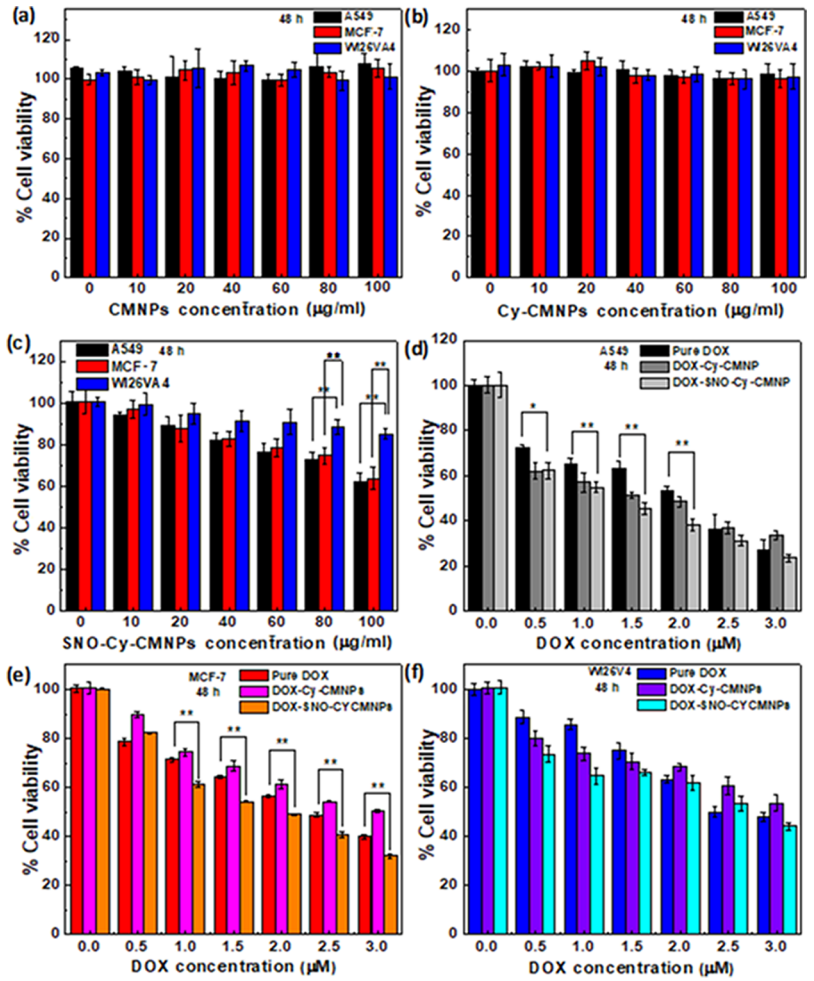

Figure 4. Viability of A549, MCF-7, and WI26VA4 cells upon incubation with (a) CMNPs, (b) Cy-CMNPs, and (c) SNO-Cy-CMNPs; viability of (d) A549, (e) MCF-7, and (f) WI26VA4 cells incubated with pure DOX, DOX-Cy-CMNPs, and DOX-SNO-Cy-CMNPs for 48h in culture conditions at 37 °C. Data represent the mean ± SD (n = 3); the statistically significant values were obtained using a t test; *p < 0.05, **p < 0.01.

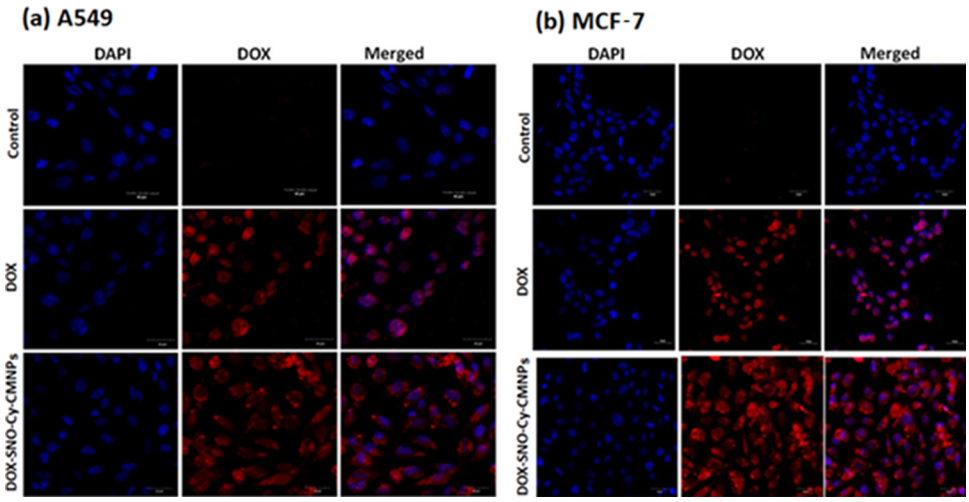

Figure 5. Confocal microscopy images of (a) A549 and (b) MCF-7 cells after incubation with DOX and DOX-SNO-Cy-CMNPs under culture conditions (DAPI was used for nuclear staining; red filter for DOX and blue filter for DAPI; scale bar: 40 μm).

revealing the shoulder at ∼350 nm is shown in Figure S1d (Supporting Information).

These nanocarriers exhibit superparamagnetic behavior at 280 K and ferrimagnetic ordering at 5 K with coercivity and remanence magnetization of 250 Oe and 12 emu/g, respectively (inset A of Figure 2c). Further, the maximum magnetizations of SNO-Cy-CMNPs were found to be 43 and 51.6 emu/g at 280 and 5 K, respectively, at an applied field of 50 kOe. It has been observed that these nanocarriers form a good colloidal dispersion in aqueous medium and are easily

https://doi.org/10.1021/acsomega.3c03734
ACS Omega 2023, 8, 44545−44557

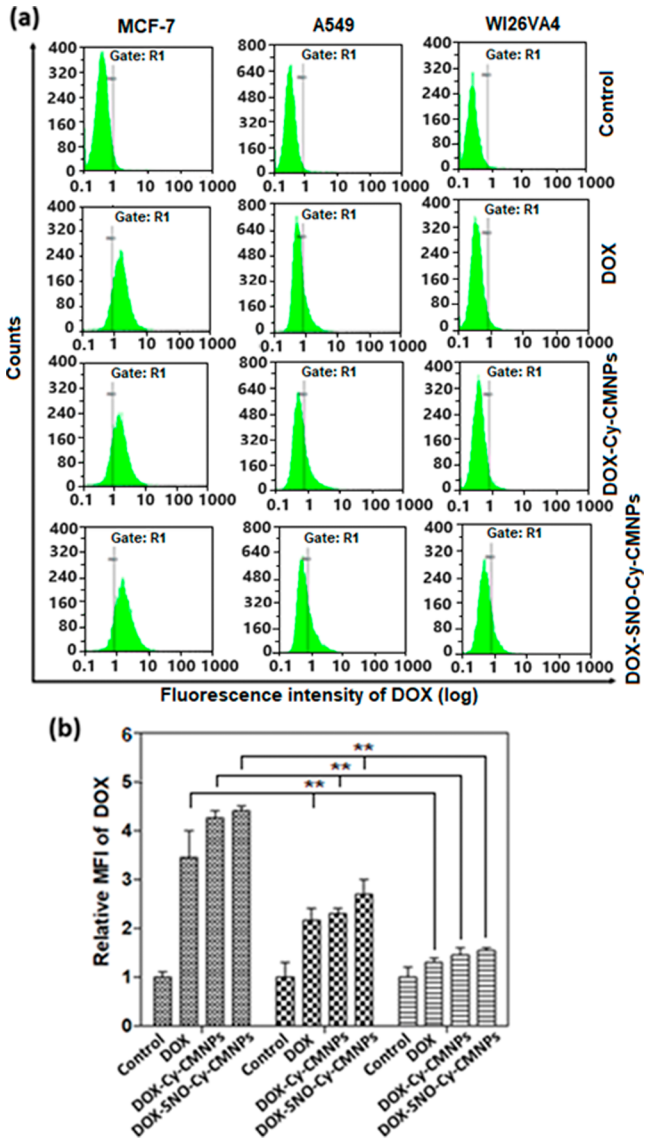

Figure 6. (a) Flow cytometric histogram and (b) MFI of different cells treated with DOX, DOX-Cy-CMNPs and DOX-SNO-Cy-CMNPs for 3 h at a DOX concentration of 5 μM under culture conditions. Data represent the mean ± SD (n = 3); the statistically significant values were obtained using a t test; $^{**}p < 0.01$.

attracted toward an external magnet of field strength 0.25 kOe (inset B of Figure 2c). The observed low value of magnetization of SNO-Cy-CMNPs as compared to bulk Fe_3O_4 (92 emu/g) can be attributed to the formation of nanosized particles as well as to the presence of nonmagnetic coating of organic molecules on their surface.[49] Further, the ZFC-FC plot shows that the blocking temperature (T_B) of the SNO-Cy-CMNPs is around 225 K, which strongly supports the observed ferrimagnetic ordering at 5 K (Figure 2d). The transition from superparamagnetic to ferrimagnetic behavior below T_B is typically observed for MNPs.

3.2. Loading and Release Studies of DOX and NO Molecules. After successful structural characterization of the magnetic nanoplatform (SNO-Cy-CMNPs), anticancer drug (DOX) was electrostatically bound to the negatively charged surface (via a carboxyl moiety). The percentage of drug loading was optimized by varying the DOX-to-particle (expressed in terms Fe concentration) ratio, and a maximum

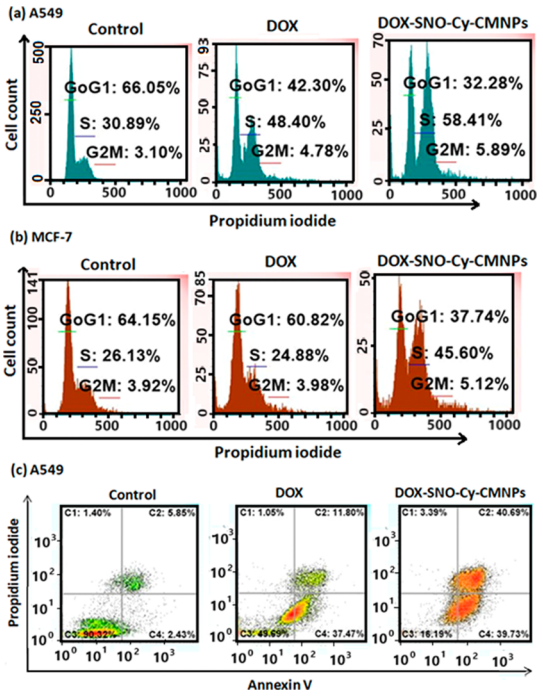

Figure 7. Cell cycle analysis of (a) A549 and (b) MCF-7 cell lines by flow cytometry after 24 h of treatment with pure DOX and DOX-SNO-Cy-CMNPs and (c) annexin V/PI staining in A549 cells for estimating the apoptosis ratio after 24 h of incubation with DOX-SNO-Cy-CMNPs and pure DOX.

loading efficiency of about 85% with a drug loading content of 3% was observed at 1:14 (Figure S2, Supporting Information). The interaction of DOX molecules with SNO-Cy-CMNPs was also evident from the decrease in absorbance of the supernatant liquid after removal of DOX-loaded SNO-Cy-CMNPs (DOX-SNO-Cy-CMNPs) as shown in Figure 3a. The affinity of DOX for negatively charged moieties such as carboxyl, phosphate, and sulfate groups has been investigated earlier by our group.[39,41] It is noteworthy to mention that the intensity-weighted average hydrodynamic diameter of the developed drug carriers (DOX-SNO-Cy-CMNPs) was found to be 135 nm (Figure S3, Supporting Information), which is well below the diameter of the blood capillary. Thus, this drug formulation can easily pass through the blood capillary, and pH sensitivity at the subcellular level can trigger the release of the drug into endosomes or lysosomes (mild acidic environment). Therefore, the release of DOX-SNO-Cy-CMNPs and pure DOX was investigated at 37 °C under reservoir-sink condition to mimic the cellular environment of the tumor (Figure 3b). It has been observed that almost 66% of the loaded drug is getting released from DOX-SNO-Cy-CMNPs slowly over a period of 72 h at pH 5.5, whereas almost 100% of the drug is released from pure DOX within 1 h. The sustained release of DOX from DOX-SNO-Cy-CMNPs could be attributed to the slow weakening/breaking of the electrostatic interactions between the drug and partially neutralized carboxyl groups present on the surface of carriers at lower pH. Further, the short time release behavior of DOX from DOX-SNO-Cy-CMNPs (Figure S4, Supporting Information) shows a linear relationship between drug release and square root of time ($t^{1/2}$) as anticipated for the Higuchi drug release model, suggesting that the DOX release process is diffusion-controlled.[50,51] It is worth mentioning that only 16.5% of

https://doi.org/10.1021/acsomega.3c03734
ACS Omega 2023, 8, 44545−44557

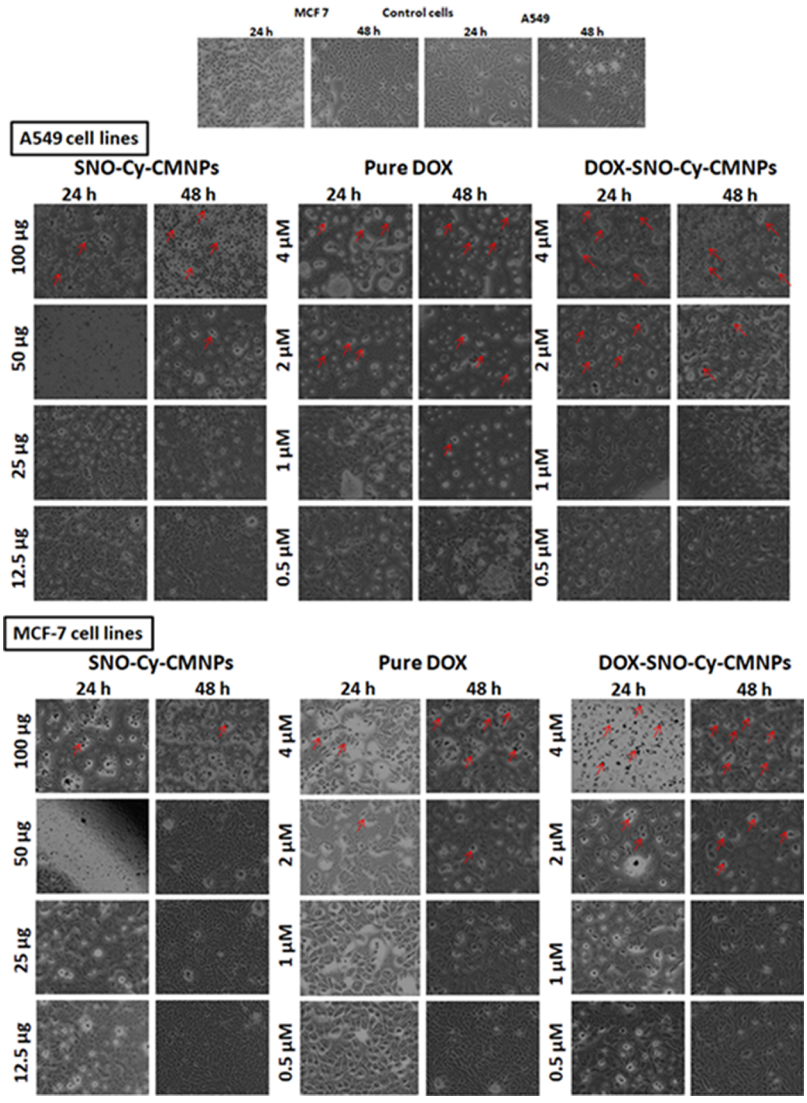

Figure 8. Bright-field microscopy images of (a) A549 and (b) MCF-7 cells after different treatments with SNO-Cy-CMNPs, pure DOX, and DOX-SNO-Cy-CMNPs at 24 and 48 h. Red arrows indicate cells depicting apoptotic morphology.

loaded DOX is released over a period of 72 h from DOX-SNO-Cy-CMNPs at pH 7.4, indicating the good stability of the developed formulation at physiological pH medium. A similar pH-dependent release of DOX (65 and 25% at pH 5 and pH 7.4, respectively) was reported by Jia et al. from DOX and Fe_3O_4 nanoparticles-coencapsulated poly (D, L-lactic-co-glycolic acid)-based polymeric nanocarrier.[52] The observed pH-dependent release of DOX with higher levels at acidic tumor sites than in plasma or normal tissues is desired for the anticancer drug-delivery system.

The well-known molecular NO donors like GSNO suffer from inadequate cellular uptake.[53] Therefore, NO molecules were introduced onto the surface of Cy-CMNPs by nitrosation of thiol groups for enhancement of their intracellular level via passive- as well as magnetic field-induced targeting. The NO loading and their cellular uptake, and release (intracellular and pH-dependent release under reservoir-sink condition) were determined through the standard curve prepared with sodium nitrite ($NaNO_2$) solution in the concentration range 10−100 μM as shown in Figure 3c using Griess reagent. By comparing with the calibration curve, the NO-loading efficiency of Cy-CMNPs was found to be around 65.5%. The intracellular NO uptake was calculated in two different time frames (4 and 24 h) in A549 and MCF-7 cell lines. The result obtained showed a time-dependent uptake of NO-releasing magnetic nanocarriers. The intracellular NO uptakes of 72.1 and 69.6 μM were observed in A549 cells after 4 h of incubation of SNO-Cy-CMNPs and DOX-SNO-Cy-CMNPs, respectively, whereas those in MCF-7 cells were found to be 62.5 and 64.5 μM. Moreover, the corresponding intracellular uptake was increased to 264.8 and 300.0 μM in A549 cells and 280.6 and 290.4 μM in MCF-7 after 24 h of incubation (Figure 3d). The amounts of NO released from SNO systems (obtained after 24 h incubation of DOX-SNO-Cy-CMNPs and SNO-Cy-CMNPs with cancer cells)-treated cancer cells was monitored. It was found that NO release in A549 and MCF-7 cells proceeds through a time-dependent manner for DOX-SNO-Cy-CMNPs and SNO-Cy-CMNPs with a maximum of 42.5 and 41.2% in A549 and 38.8 and 38.6% in MCF-7 cells, respectively. (Figure 3e). The pH-dependent NO release profile was also investigated over a period of 24 h in the cellular mimicking environment under reservoir-sink condition, and it was found that NO release is pH independent in the experimental range of 7.4−5.5.[54] A cumulative release of 35.0

https://doi.org/10.1021/acsomega.3c03734
ACS Omega 2023, 8, 44545−44557

and 39.4% of NO was observed after 24 h at pH 7.4 and 5.5, respectively (Figure 3f). It is believed that the NO released from DOX-SNO-Cy-CMNPs and SNO-Cy-CMNPs mainly occurred through the homolytic cleavage of S−N bond.[55] In general, at elevated levels of glutathione (GSH), the intracellular NO donors (S-NO) were degraded in NO and NH_3 depending upon the GSH concentration.

3.3. Cytotoxicity, Cellular Uptake, and Cell Cycle Analysis Studies. Cytotoxicity of CMNPs (used as core material for preparation of Cy-CMNPs) and Cy-CMNPs (used as nanocarriers for NO and DOX) was investigated on normal (WI26VA4) and cancer (A549 and MCF-7) cell lines after 48 h of incubation by the MTT assay. Both CMNPs and Cy-CMNPs were found to be nontoxic toward normal (WI26VA4) and cancer (A549 and MCF-7) cell lines even up to 100 μg/mL concentration (Figure 4a,b). This result indicates that our nanocarriers are biocompatible and do not have significant adverse toxicity. It is noteworthy to mention that more than 90% of WI26VA4 cells were viable even after 48 h of incubation with 80 μg/mL of NO-loaded system (SNO-Cy-CMNPs), whereas A549 and MCF-7 cells have realized significant toxicity suggesting the effect of NO (Figure 4c) over cancer cell lines. A similar cytotoxicity result was observed by Seabra et al., where S-nitrosated-coated particles exhibited higher toxicity effects over thiol-coated iron-oxide nanoparticles.[56]

Further, the cytotoxicity effect of pure DOX and DOX-loaded systems (DOX-Cy-CMNPs and DOX-SNO-Cy-CMNPs) was also explored on A549, MCF-7, and WI26VA4 cell lines after 48 h of incubation (Figure 4d−f). The developed DOX-loaded systems retained the cytotoxicity effect of the drug, and a concentration-dependent toxicity is observed toward proliferation of cells. It has been observed that DOX-SNO-Cy-CMNPs showed higher toxicity than without nitroso-modified counterpart (DOX-Cy-CMNPs), indicating the positive role of NO in the killing of cancer cells. The IC_{50} values of DOX-SNO-Cy-CMNPs and DOX-Cy-CMNPs in A549 cell were found to be 1.06 and 1.34 μM, respectively, and that of pure DOX was 1.75 μM. In the case of MCF-7 cells, the IC_{50} values were 1.72 and 2.98 μM for DOX-SNO-Cy-CMNPs and DOX-Cy-CMNPs, respectively, and that of pure DOX was 2.36 μM. Thus, the present studies clearly indicate the effect of NO in augmenting the cell-killing efficacy. Similarly, Song et al.[57] and Alimoradi et al.[58] reported the enhancement in the antitumor efficacy for NO and DOX-loaded nanocarriers.

Moreover, our developed nanocarriers (DOX-SNO-Cy-CMNPs) showed significantly lower cytotoxicity (>20%) at higher concentrations in WI26VA4, suggesting their relatively selective toxicity to cancer cells than normal cells. However, the observed toxicity of DOX-SNO-Cy-CMNPs in normal cells than SNO-Cy-CMNPs (without conjugation of DOX) may be attributed to the presence of DOX, which may impose higher inherent toxicity in normal cells.[59]

To investigate the cellular internalization, confocal microscopic studies were carried out on A549 (Figure 5a) and MCF-7 (Figure 5b) cells after incubation with DOX and DOX-SNO-Cy-CMNPs under culture conditions. The cells without exposure to DOX and DOX-SNO-Cy-CMNPs were used as a negative control and showed only autofluorescence from cells. The blue color fluorescence emission arises from the DAPI-stained nuclei. A considerable uptake of DOX-SNO-Cy-CMNPs was evident from the red color fluorescence emission coming from DOX. The magenta color emission originating from the merged image of DOX and DAPI fluorescence clearly suggests that pure DOX shows mainly nuclear internalization, whereas DOX-SNO-Cy-CMNPs are localized in the cytoplasm. Further, the confocal microscopy images of WI26VA4 cells (Figure S5, Supporting Information) were also acquired after incubation with DOX and DOX-SNO-Cy-CMNPs. Though the uptake of DOX in WI26VA4 cells was evident from confocal microscopic studies, its fluorescence signal intensity was found to be less than that A549 and MCF-7 cell lines. This result further supports the higher uptake of DOX-SNO-Cy-CMNPs in cancer cells over normal cells. We believed that DOX-SNO-Cy-CMNPs directly transferred to the cytoplasm by internalization through membrane penetration (passively targeted to the tumors via EPR effect).[60] It is well-reported that the nanocarriers cannot pass through the tight junction between normal vascular linings, whereas the leaky vasculature of the cancer region favors their uptake. Moreover, being magnetic in nature, the developed nanocarriers can be targeted to the tumor site by applying an external magnetic field.

The uptake of DOX, DOX-Cy-CMNPs, and DOX-SNO-Cy-CMNPs in A549, MCF-7, and WI26VA4 cells was further verified by flow cytometric analysis. The flow cytometric histogram and the corresponding mean fluorescence intensity (MFI) of different cells treated with DOX, DOX-Cy-CMNPs, and DOX-SNO-Cy-CMNPs are shown in Figure 6a,b, respectively. Compared to the control, a distinguishable increase in the fluorescence intensity was observed in all of the above cells treated with pure DOX and DOX-loaded systems. However, the increase in fluorescence intensity is higher in cancer cell lines (A549 and MCF-7) over normal cells (WI26VA4). Further, it has been observed that the fluorescence intensity from cells treated with DOX-SNO-Cy-CMNPs was more than that of cells treated with DOX-Cy-CMNPs. This study mainly suggests a higher uptake of DOX-SNO-Cy-CMNPs in cancer cells. However, the cellular uptake of nonfluorescent SNO-Cy-CNPs (without DOX) as well as DOX-SNO-Cy-CMNPs was also confirmed from the bright-field microscopy imaging (Figure S6 Supporting Information), where the black-colored Fe_3O_4 nanoparticle deposition is clearly visible in and around treated A549 cells, which was not seen in control cells.

To identify the mechanism of cell death induced by DOX-SNO-Cy-CMNPs, Sub-G1 analysis was performed by flow cytometry after PI staining (Figure 7a,b). Results showed that control cells without any treatment were mostly found to be in the G0/G1 phase and S phase of the cell cycle in both A549 and MCF-7 cell lines. Treatment with pure DOX (5 μM) showed an increase in the accumulation of cells in the S phase (48.40%) of the cell cycle in A549 cells. On the other hand, treatment with DOX-SNO-Cy-CMNPs caused significantly higher accumulation of cells in the S phase of the cell cycle such as 58.41 and 45.60% in A549 and MCF-7, respectively, after 24 h of treatment. To further validate the contribution of apoptosis in DOX-SNO-Cy-CMNPs mediated enhanced cell death, a more specific assay for apoptosis, annexin V/PI staining, was carried out at 24 h (Figure 7c). Untreated cells showed subtle or no annexin V expression, indicating no apoptosis induction, whereas treatment of DOX and DOX-SNO-Cy-CMNPs showed significant levels of annexin V expression in comparison to the control, which has indicated robust apoptosis induction in A549 cells. Notably, treatment of DOX-SNO-Cy-CMNPs showed more than 40% increase in

https://doi.org/10.1021/acsomega.3c03734
ACS Omega 2023, 8, 44545−44557

late apoptotic cells with annexin V expression and PI uptake. On other hand, cells treated with only DOX showed relatively slower cell death, as was observed in the low percentage of cells with PI expression. Thus, this result indicated the tumor suppressive role of NO in augmenting the cell-killing efficacy of DOX in inducing apoptosis in cancer cells. Similarly, Xia et al.[61] and Li et al.[62] reported higher antiproliferative effect of DOX loaded in selenium nanoparticles and DOX-loaded polyglycerol-nanodiamond composites on U87 GBM cell line over pure DOX.

Bright-field microscopy images also confirmed the presence of cells depicting apoptotic morphology (cellular detachment, circularization, and change in opacity) in DOX-SNO-Cy-CMNPs-treated A549 and MCF-7 cells (Figure 8a,b). It is clearly visible that the cells treated with pure DOX and DOX-SNO-Cy-CMNPs have shown time- and concentration-dependent cellular apoptosis which are marked by red arrows. With increasing concentration, incremental change of cellular morphology was observed in both cell lines postulating the higher induction of apoptosis by DOX-SNO-Cy-CMNP nanoplatform. Thus, after all this rigorous cellular study, it can be ascertained that the induction of apoptosis is the major cell death pathway induced by DOX-SNO-Cy-CMNPs nanoplatform in both the cancer cells as validated by cell cycle analysis and annexin V/PI assay. Moreover, these nanocarriers do not exhibit any significant change in absorbance (Figure S7, Supporting Information) as well as zeta potential (Table S1, Supporting Information) even after interacting with the BSA protein in a physiological medium (0.01 M PBS, pH 7.4). This suggests the protein resistance characteristic of the developed NO-releasing nanocarriers in a physiological medium, which is essential for their therapeutic applications.

4. CONCLUSIONS

In summary, a highly water dispersible magnetic nanoplatform was developed by precise surface modification for dual delivery of NO and the chemotherapeutic drug, DOX. These smart magnetic nanocarriers exhibited good water dispersibility and enhanced the stability of NO in PBS and cellular mediums. They showed sustained release of both DOX and NO, and the passive targeting capacity of the developed nanocarriers was found to significantly inhibit the growth of human lung cancer cell (A549) and human breast cancer (MCF-7) cell lines in a concentration-dependent manner. The codelivery of NO along with DOX was found to increase the late apoptotic cell death in DOX-loaded NO-releasing nanoplatform (DOX-SNO-Cy-CMNPs) in comparison to free DOX molecules. Thus, the developed NO prodrug based on smart magnetic carriers can be utilized as a promising pH-sensitive platform for achieving the combinatorial effect of NO and chemotherapeutic drugs for effective killing of cancer cells. In the future, the in vivo antitumor effect using various tumor models will be performed.

■ ASSOCIATED CONTENT

Supporting Information

The Supporting Information is available free of charge at https://pubs.acs.org/doi/10.1021/acsomega.3c03734.

Colloidal stability, UV−visible absorption spectra, drug loading and drug release kinetics, particle size distribution, confocal images of normal cell lines and bright-field microscopy images of cancer cells, and protein-particle interaction (PDF)

■ AUTHOR INFORMATION

Corresponding Authors

Kanhu C. Barick − *Chemistry Division, Bhabha Atomic Research Centre, Trombay, Mumbai 400085, India; Homi Bhabha National Institute, Mumbai 400094, India;* orcid.org/0000-0002-9566-6870; Phone: + 91 22 2559 0284; Email: kcbarick@barc.gov.in; Fax: + 91 22 2550 5151

Puthussericka A. Hassan − *Chemistry Division, Bhabha Atomic Research Centre, Trombay, Mumbai 400085, India; Homi Bhabha National Institute, Mumbai 400094, India;* orcid.org/0000-0001-7137-4788; Phone: + 91 22 2559 0284; Email: hassan@barc.gov.in; Fax: + 91 22 2550 5151

Authors

Bijaideep Dutta − *Chemistry Division, Bhabha Atomic Research Centre, Trombay, Mumbai 400085, India; Homi Bhabha National Institute, Mumbai 400094, India*

Sandeep B. Shelar − *Chemistry Division, Bhabha Atomic Research Centre, Trombay, Mumbai 400085, India;* orcid.org/0000-0001-6404-8028

Ananya Nirmalraj − *Chemistry Division, Bhabha Atomic Research Centre, Trombay, Mumbai 400085, India; Department of Chemistry, Sunandan Divatia School of Science, SVKM's NMIMS (Deemed-to-be University), Mumbai 400056, India*

Sonali Gupta − *Chemistry Division, Bhabha Atomic Research Centre, Trombay, Mumbai 400085, India; Homi Bhabha National Institute, Mumbai 400094, India*

Jagriti Gupta − *Chemistry Division, Bhabha Atomic Research Centre, Trombay, Mumbai 400085, India*

Complete contact information is available at: https://pubs.acs.org/10.1021/acsomega.3c03734

Notes

The authors declare no competing financial interest.

■ ACKNOWLEDGMENTS

The authors acknowledge Dr. A. K. Tyagi, Director Chemistry Group, Bhabha Atomic Research Centre (BARC), India for his constant support and encouragement. The authors also thank Dr. H. G. Salunke, TPD, BARC for magnetization measurements. One of the authors, Dr. J.G., thanks the BARC and the Department of Science and Technology, India (grant No. SR/WOS-A/CS-146/2018) for support of this work.

■ REFERENCES

(1) Sung, H.; Ferlay, J.; Siegel, R. L.; Laversanne, M.; Soerjomataram, I.; Jemal, A.; Bray, F. Global Cancer Statistics 2020: GLOBOCAN Estimates of Incidence and Mortality Worldwide for 36 Cancers in 185 Countries. *CA Cancer J. Clin.* **2021**, *71* (3), 209−249.

(2) Tan, K.; Lian, L.; Palanirajan, V. K. Surface Functionalization of Gold Nanoparticles for Targeting the Tumor Microenvironment to Improve Antitumor Efficiency. *ACS Appl. Bio Mater.* **2023**, *6* (8), 2944−2981.

(3) Li, T.; Wu, M.; Wei, Q.; Xu, D.; He, X.; Wang, J.; Wu, J.; Chen, L. Conjugated Polymer Nanoparticles for Tumor Theranostics. *Biomacromolecules* **2023**, *24* (5), 1943−1979.

(4) Mohajer, F.; Mirhosseini-Eshkevari, B.; Ahmadi, S.; Ghasemzadeh, M. A.; Ziarani, G. M.; Badiei, A.; Farshidfar, N.; Varma, R. S.; Rabiee, N.; Iravani, S. Advanced Nanosystems for Cancer Therapeutics: A Review. *ACS Appl. Nano Mater.* **2023**, *6* (9), 7123−7149.
(5) Kashyap, B. K.; Singh, V.; Solanki, M. K.; Kumar, A.; Ruokolainen, J.; Kesari, K. K. Smart Nanomaterials in Cancer Theranostics: Challenges and Opportunities. *ACS Omega* **2023**, *8* (16), 14290−14320.
(6) Ale, Y.; Nainwal, N. Progress and Challenges in the Diagnosis and Treatment of Brain Cancer Using Nanotechnology. *Mol. Pharmaceutics* **2023**, *20*, 4893.
(7) Khan, M. M.; Torchilin, V. P. Recent Trends in Nanomedicine-Based Strategies to Overcome Multidrug Resistance in Tumors. *Cancers* **2022**, *14* (17), 4123.
(8) Katmerlikaya, T. G.; Dağ, A.; Özgen, P. S. O.; Ersen, B. C. Dual-Drug Conjugated Glyco-Nanoassemblies for Tumor-Triggered Targeting and Synergistic Cancer Therapy. *ACS Appl. Bio Mater.* **2022**, *5* (11), 5356−5364.
(9) Barman, R.; Bej, R.; Dey, P.; Ghosh, S. Cisplatin-Conjugated Polyurethane Capsule for Dual Drug Delivery to a Cancer Cell. *ACS Appl. Mater. Interfaces* **2023**, *15* (21), 25193−25200.
(10) Dutta, B.; Nema, A.; Shetake, N. G.; Gupta, J.; Barick, K. C.; Lawande, M. A.; Pandey, B. N.; Priyadarsini, I. K.; Hassan, P. A. Glutamic Acid-Coated Fe_3O_4 Nanoparticles for Tumor-Targeted Imaging and Therapeutics. *Mater. Sci. Eng. C* **2020**, *112*, No. 110915, DOI: 10.1016/j.msec.2020.110915.
(11) Alam, A.; Karmakar, R.; Rengan, A. K.; Khandelwal, M. Nanofiber-Based Systems for Stimuli-Responsive and Dual Drug Delivery: Present Scenario and the Way Forward. *ACS Biomater. Sci. Eng.* **2023**, *9* (6), 3160−3184.
(12) Shao, N.; Yuan, L.; Ma, P.-C.; Zhou, M.; Xiao, X.; Cong, Z.; Wu, Y.; Xiao, G.; Fei, J.; Liu, R.-H. Heterochiral β-Peptide Polymers Combating Multidrug-Resistant Cancers Effectively without Inducing Drug Resistance. *J. Am. Chem. Soc.* **2022**, *144* (16), 7283−7294, DOI: 10.1021/jacs.2c00452.
(13) Ignarro, L. J. Nitric Oxide: A Unique Endogenous Signaling Molecule in Vascular Biology. *Angew. Chem., Int. Ed.* **1999**, *38* (13−14), 1882−1892.
(14) Lundberg, J. O.; Weitzberg, E. Nitric Oxide Signaling in Health and Disease. *Cell* **2022**, *185* (16), 2853−2878.
(15) Stuehr, D. J. Structure-Function Aspects in the Nitric Oxide Synthases. *Ann. Rev. Pharmacol. Toxicol.* **1997**, *37* (1), 339−359.
(16) Heinrich, T. A.; da Silva, R. S.; Miranda, K. M.; Switzer, C. H.; Wink, D. A.; Fukuto, J. M. Biological Nitric Oxide Signalling: Chemistry and Terminology. *Br. J. Pharmacol.* **2013**, *169* (7), 1417−1429.
(17) Lundberg, J. O.; Gladwin, M. T.; Weitzberg, E. Strategies to Increase Nitric Oxide Signalling in Cardiovascular Disease. *Nat. Rev. Drug Discov.* **2015**, *14* (9), 623−641.
(18) Premont, R. T.; Singel, D. J.; Stamler, J. S. The Enzymatic Function of the Honorary Enzyme: S-Nitrosylation of Hemoglobin in Physiology and Medicine. *Mol. Aspects Med.* **2022**, *84*, No. 101056.
(19) Bahadoran, Z.; Mirmiran, P.; Ghasemi, A. Role of Nitric Oxide in Insulin Secretion and Glucose Metabolism. *Trends Endocrinol. Metabol.* **2020**, *31* (2), 118−130.
(20) Garthwaite, J. NO as a Multimodal Transmitter in the Brain: Discovery and Current Status. *Br. J. Pharmacol.* **2019**, *176* (2), 197−211.
(21) Cinelli, M. A.; Do, H. T.; Miley, G. P.; Silverman, R. B. Inducible Nitric Oxide Synthase: Regulation, Structure, and Inhibition. *Med. Res. Rev.* **2020**, *40* (1), 158−189.
(22) Das, R. P.; Singh, B. G.; Aishwarya, J.; Kumbhare, L. B.; Kunwar, A. 3,3′-Diselenodipropionic Acid Immobilised Gelatin Gel: A Biomimic Catalytic Nitric Oxide Generating Material for Topical Wound Healing Application. *Biomater. Sci.* **2023**, *11* (4), 1437−1450.
(23) Wang, Z.; Jin, A. J.; Yang, Z.; Huang, W. Advanced Nitric Oxide Generating Nanomedicine for Therapeutic Applications. *ACS Nano* **2023**, *17* (10), 8935−8965.
(24) Carpenter, A. W.; Schoenfisch, M. H. Nitric Oxide Release: Part II. Therapeutic Applications. *Chem. Soc. Rev.* **2012**, *41* (10), 3742.
(25) Liu, Y.; Wang, X.; Li, J.; Tang, J.; Li, B.; Zhang, Y.; Gu, N.; Yang, F. Sphingosine 1-Phosphate Liposomes for Targeted Nitric Oxide Delivery to Mediate Anticancer Effects against Brain Glioma Tumors. *Adv. Mater.* **2021**, *33* (30), No. e2101701.
(26) Li, G.; Lu, X.; Zhang, S.; Zhang, J.; Fu, X.; Zhang, M.; Teng, L.; Sun, F. Multi-Enzyme Cascade-Triggered Nitric Oxide Release Nanoplatform Combined with Chemo Starvation-like Therapy for Multidrug-Resistant Cancers. *ACS Appl. Mater. Interfaces* **2023**, *15* (26), 31285−31299.
(27) Chung, M.; Liu, H.; Lin, K.; Chia, W.; Sung, H. A PH-Responsive Carrier System That Generates NO Bubbles to Trigger Drug Release and Reverse P-Glycoprotein-Mediated Multidrug Resistance. *Angew. Chem., Int. Ed.* **2015**, *54* (34), 9890−9893.
(28) Yu, W.; Liu, T.; Zhang, M.; Wang, Z.; Ye, J.; Li, C.-X.; Liu, W.; Li, R.; Feng, J.; Zhang, X.-Z. O_2 Economizer for Inhibiting Cell Respiration to Combat the Hypoxia Obstacle in Tumor Treatments. *ACS Nano* **2019**, *13*, 1784 DOI: 10.1021/acsnano.8b07852.
(29) Deng, Y.; Wang, Y.; Jia, F.; Liu, W.; Zhou, D.; Jin, Q.; Ji, J. Tailoring Supramolecular Prodrug Nanoassemblies for Reactive Nitrogen Species-Potentiated Chemotherapy of Liver Cancer. *ACS Nano* **2021**, *15* (5), 8663−8675.
(30) Hu, C.; Cun, X.; Ruan, S.; Liu, R.; Xiao, W.; Yang, X.; Yang, Y.; Yang, C.; Gao, H. Enzyme-Triggered Size Shrink and Laser-Enhanced NO Release Nanoparticles for Deep Tumor Penetration and Combination Therapy. *Biomaterials* **2018**, *168*, 64−75.
(31) Chen, M.; Song, F.; Liu, Y.; Tian, J.; Liu, C.; Li, R.; Zhang, Q. A Dual PH-Sensitive Liposomal System with Charge-Reversal and NO Generation for Overcoming Multidrug Resistance in Cancer. *Nanoscale* **2019**, *11* (9), 3814−3826.
(32) Dong, X.; Liu, H.-J.; Feng, H.-Y.; Yang, S.-C.; Liu, X.-L.; Lai, X.; Lu, Q.; Lovell, J. F.; Chen, H.-Z.; Fang, C. Enhanced Drug Delivery by Nanoscale Integration of a Nitric Oxide Donor to Induce Tumor Collagen Depletion. *Nano Lett.* **2019**, *19* (2), 997−1008.
(33) Cao, Y.; Liu, M.; Cheng, J.; Yin, J.; Huang, C.; Cui, H.; Zhang, X.; Zhao, G. Acidity-Triggered Tumor-Targeted Nanosystem for Synergistic Therapy via a Cascade of ROS Generation and NO Release. *ACS Appl. Mater. Interfaces* **2020**, *12*, 28975 DOI: 10.1021/acsami.0c04791.
(34) Lee, J.; Hlaing, S. P.; Hasan, N.; Kwak, D.; Kim, H. W.; Cao, J.; Yoon, I.; Yun, H.; Jung, Y.; Yoo, J. Tumor-Penetrable Nitric Oxide-Releasing Nanoparticles Potentiate Local Antimelanoma Therapy. *ACS Appl. Mater. Interfaces* **2021**, *13* (26), 30383−30396.
(35) Yuan, X.; Zhao, X.; Xia, R.; Xie, Z.; Lin, Y.; Su, Z. Photothermally responsive magnetic nanoparticles for nitric oxide release to combat *Staphylococcus aureus* biofilms. *ACS Appl. Nano Mater.* **2022**, *5* (12), 18799−18810.
(36) Yu, B.; Deng, Y.; Jia, F.; Wang, Y.; Jin, Q.; Ji, J. A Supramolecular Nitric Oxide Nanodelivery System for Prevention of Tumor Metastasis by Inhibiting Platelet Activation and Aggregation. *ACS Appl. Mater. Interfaces* **2022**, *14* (43), 48515−48526.
(37) Liu, Z.; Zhou, Y.; Huang, X.; Zhou, J.; Huang, D.; Li, Y.; Wang, Z.; Dong, B.; Qiao, H.; Chen, W. Inherently nitric oxide containing polymersomes remotely regulated by NIR for improving multi-modal therapy on drug resistant cancer. *Biomaterials* **2021**, *277*, No. 121118.
(38) Santos, M. C.; Seabra, A. B.; Pelegrino, M. T.; Haddad, P. S. Synthesis, Characterization and Cytotoxicity of Glutathione- and PEG-Glutathione-Superparamagnetic Iron Oxide Nanoparticles for Nitric Oxide Delivery. *Appl. Surf. Sci.* **2016**, *367*, 26−35.
(39) Nigam, S.; Barick, K. C.; Bahadur, D. Development of Citrate-Stabilized Fe_3O_4 Nanoparticles: Conjugation and Release of Doxorubicin for Therapeutic Applications. *J. Magn. Magn. Mater.* **2011**, *323* (2), 237−243.
(40) Zhang, J.; Song, H.; Ji, S.; Wang, X.; Huang, P.; Zhang, C.; Wang, W.; Kong, D. NO Prodrug-Conjugated, Self-Assembled, pH-Responsive and Galactose Receptor Targeted Nanoparticles for Co-

Delivery of Nitric Oxide and Doxorubicin. *Nanoscale* **2018**, *10* (9), 4179−4188.
(41) Majeed, J.; Barick, K. C.; Shetake, N. G.; Pandey, B. N.; Hassan, P. A.; Tyagi, A. K. Water-Dispersible Polyphosphate-Grafted Fe_3O_4 Nanomagnets for Cancer Therapy. *RSC Adv.* **2015**, *5* (105), 86754−86762.
(42) Dutta, B.; Shelar, S. B.; Barick, K. C.; Shetty, P.; Chakravarty, R.; Chakraborty, S.; Checker, S.; Sarma, H. D.; Hassan, P. A. Surface engineered Fe_3O_4 nanomagnets for pH-responsive delivery of gemcitabine hydrochloride and in-vivo tracking by radiolabeling. *Mater. Adv.* **2023**, *4*, 195−204.
(43) Dutta, B. K.; Shetake, N. G.; Barick, B. K.; Barick, K. C.; Pandey, B. N.; Priyadarsini, K. Indira; Hassan, P. A. PH Sensitive Surfactant-Stabilized Fe3O4Magnetic Nanocarriers for Dual Drug Delivery. *Colloids Surf., B* **2018**, *162*, 163−171.
(44) Adhikari, M.; Echeverria, E.; Risica, G.; McIlroy, D. N.; Nippe, M.; Vasquez, Y. Synthesis of Magnetite Nanorods from the Reduction of Iron OxyHydroxide with Hydrazine. *ACS Omega* **2020**, *5*, 22440−22448.
(45) Li, L.; Liao, L.; Ding, Y.; Zeng, H. Dithizone-Etched CdTe Nanoparticles-Based Fluorescence Sensor for the Off−on Detection of Cadmium Ion in Aqueous Media. *RSC Adv.* **2017**, *7* (17), 10361−10368.
(46) Barick, K. C.; Varaprasad, B. S. D. C. S.; Singh, B. P.; Bahadur, D. Fe^{3+} doped SiO_2 nanostructured gel-glasses: Structural, optical and magnetic properties. *J. Non-Cryst. Solids* **2005**, *351*, 3693−3698.
(47) Sojková, T.; Rizzo, G. M. R.; Girolamo, A. D.; Avugadda, S. K.; Soni, N.; Milbrandt, N. B.; Tsai, Y. H.; Kuběna, I.; Sojka, M.; Silvestri, N.; Samia, A. C.; Gröger, R.; Pellegrino, T. From Core−Shell FeO/Fe_3O_4 to Magnetite Nanocubes: Enhancing Magnetic Hyperthermia and Imaging Performance by Thermal Annealing. *Chem. Mater.* **2023**, *35* (16), 6201−6219.
(48) Wu, F.; Sun, B.; Chu, X.; Zhang, Q.; She, Z.; Song, S.; Zhou, N.; Zhang, J.; Yi, X.; Wu, D.; Wang, J. Hyaluronic Acid-Modified Porous Carbon-Coated Fe3O4 Nanoparticles for Magnetic Resonance Imaging-Guided Photothermal/Chemotherapy of Tumors. *Langmuir* **2019**, *35* (40), 13135−13144.
(49) Mikhaylova, M.; Kim, K. H.; Bobrysheva, N. P.; Osmolowsky, M. G.; Semenov, V. A.; Tsakalakos, T.; Muhammed, M. Superparamagnetism of Magnetite Nanoparticles: Dependence on Surface Modification. *Langmuir* **2004**, *20* (6), 2472−2477.
(50) Mahmud, M.; Rahman, A. F. M. M.; Salem, K. S.; Bari, M. L.; Qiu, H. Architecting Ultrathin Graphitic c3N4 Nanosheets Incorporated PVA/Gelatin Bionanocomposite for Potential Biomedical Application: Effect on Drug Delivery, Release Kinetics, and Antibacterial Activity. *ACS Appl. Bio Mater.* **2022**, *5* (11), 5126−5139.
(51) Akbar, M. U.; Badar, M.; Zaheer, M. Programmable Drug Release from a Dual-Stimuli Responsive Magnetic Metal−Organic Framework. *ACS Omega* **2022**, *7*, 32588.
(52) Jia, Y.; Yuan, M.; Yuan, H.; Huang, X.; Sui, X.; Cui, X.; Tang, F.; Peng, J.; Chen, J.; Lu, S.; Xu, W. Co-Encapsulation of Magnetic Fe_3O_4 Nanoparticles and Doxorubicin into Biodegradable PLGA Nanocarriers for Intratumoral Drug Delivery. *Int. J. Nanomed.* **2012**, *7*, 1697.
(53) Seabra, A. B.; Justo, G. Z.; Haddad, P. S. State of the Art, Challenges and Perspectives in the Design of Nitric Oxide-Releasing Polymeric Nanomaterials for Biomedical Applications. *Biotechnol. Adv.* **2015**, *33* (6), 1370−1379.
(54) Wang, M.-R.; Chiu, S.-J.; Chou, H.-C.; Hu, T.-M. An Efficient S-NO-Polysilsesquioxane Nano-Platform for the Co-Delivery of Nitric Oxide and an Anticancer Drug. *Chem. Commun.* **2015**, *51* (86), 15649−15652.
(55) Shishido, M.; Seabra, A. B.; Loh, W.; Ganzarolli de Oliveira, M. Thermal and Photochemical Nitric Oxide Release from S-Nitrosothiols Incorporated in Pluronic F127 Gel: Potential Uses for Local and Controlled Nitric Oxide Release. *Biomaterials* **2003**, *24* (20), 3543−3553.
(56) Seabra, A. B.; Pasquôto, T.; Ferrarini, A. C. F.; da Santos, M. C.; Haddad, P. S.; de Lima, R. Preparation, Characterization, Cytotoxicity, and Genotoxicity Evaluations of Thiolated- and S-Nitrosated Superparamagnetic Iron Oxide Nanoparticles: Implications for Cancer Treatment. *Chem. Res. Toxicol.* **2014**, *27* (7), 1207−1218.
(57) Song, Q.; Tan, S.; Zhuang, X.; Guo, Y.; Zhao, Y.; Wu, T.; Ye, Q.; Si, L.; Zhang, Z. Nitric Oxide Releasing D-α-Tocopheryl Polyethylene Glycol Succinate for Enhancing Antitumor Activity of Doxorubicin. *Mol. Pharmaceutics* **2014**, *11* (11), 4118−4129.
(58) Alimoradi, H.; Greish, K.; Barzegar-Fallah, A.; ALshaibani, L.; Pittalà, V. Nitric Oxide-Releasing Nanoparticles Improve Doxorubicin Anticancer Activity. *Int. J. Nanomed.* **2018**, *13*, 7771−7787.
(59) Gawali, S. L.; Barick, K. C.; Shetake, N. G.; Rajan, V.; Pandey, B. N.; Kumar, N.; Priyadarsini, K. I.; Hassan, P. A. PH-Labile Magnetic Nanocarriers for Intracellular Drug Delivery to Tumor Cells. *ACS Omega* **2019**, *4* (7), 11728−11736.
(60) Dutta, B.; Barick, K. C.; Hassan, P. A. Recent Advances in Active Targeting of Nanomaterials for Anticancer Drug Delivery. *Adv. Colloid Interface Sci.* **2021**, *296*, No. 102509.
(61) Xia, Y.; Zhong, J.-Y.; Zhao, M.; Tang, Y.; Han, N.; Hua, L.; Xu, T.; Wang, C.; Zhu, B. Galactose-Modified Selenium Nanoparticles for Targeted Delivery of Doxorubicin to Hepatocellular Carcinoma. *Drug Deliv.* **2019**, *26* (1), 1−11.
(62) Li, T.; Li, K.; Zhang, Q.; Wang, C.; Yue, Y.; Chen, Z.; Yuan, S.-J.; Liu, X.; Wen, Y.; Han, M.; Komatsu, N.; Xu, Y.; Zhao, L.; Chen, X. Dendritic Cell-Mediated Delivery of Doxorubicin-Polyglycerol-Nanodiamond Composites Elicits Enhanced Anti-Cancer Immune Response in Glioblastoma. *Biomaterials* **2018**, *181*, 35−52.

https://doi.org/10.1021/acsomega.3c03734
ACS Omega 2023, 8, 44545−44557